



**HAL**  
open science

## Domain-wall-induced electromagnons in multiferroics

S Sayedaghaee, Sergey Prosandeev, Sergei Prokhorenko, Yousra Nahas,  
Charles Paillard, Bin Xu, L Bellaiche

► **To cite this version:**

S Sayedaghaee, Sergey Prosandeev, Sergei Prokhorenko, Yousra Nahas, Charles Paillard, et al..  
Domain-wall-induced electromagnons in multiferroics. *Physical Review Materials*, 2022, 6 (3),  
pp.034403. 10.1103/PhysRevMaterials.6.034403 . hal-03618401

**HAL Id: hal-03618401**

**<https://centralesupelec.hal.science/hal-03618401>**

Submitted on 24 Mar 2022

**HAL** is a multi-disciplinary open access archive for the deposit and dissemination of scientific research documents, whether they are published or not. The documents may come from teaching and research institutions in France or abroad, or from public or private research centers.

L'archive ouverte pluridisciplinaire **HAL**, est destinée au dépôt et à la diffusion de documents scientifiques de niveau recherche, publiés ou non, émanant des établissements d'enseignement et de recherche français ou étrangers, des laboratoires publics ou privés.

1           **Domain-wall-induced electromagnons in multiferroics**

2           S. Omid Sayedaghaee,<sup>1</sup> Sergey Prosandeev,<sup>1</sup> Sergei Prokhorenko,<sup>1</sup>

3           Yousra Nahas,<sup>1</sup> Charles Paillard,<sup>2</sup> Bin Xu,<sup>3</sup> and L. Bellaiche<sup>1</sup>

4           <sup>1</sup>*Physics Department and Institute for Nanoscience and Engineering,*  
5           *University of Arkansas, Fayetteville, Arkansas 72701, USA*

6           <sup>2</sup>*Laboratoire Structures, Propriétés et Modélisation des Solides,*  
7           *CentraleSupélec, CNRS UMR 8580,*

8           *Université Paris-Saclay, 91190 Gif-sur-Yvette, France*

9           <sup>3</sup>*Institute of Theoretical and Applied Physics*  
10           *and School of Physical Science and Technology,*  
11           *Soochow University, Suzhou, Jiangsu 215006, China*

12           (Dated: February 26, 2022)

## Abstract

13

14 Using an atomistic approach, we predict the emergence of new hybrid quasi-particles, namely  
15 *domain-wall-induced* electromagnons, that arise from dynamical couplings between magnons and  
16 optical phonons in systems possessing ferroelectric domain walls. These quasi-particles induce  
17 THz resonances in magnetoelectric responses and preferentially localize either near the domain  
18 walls or near the middle of domains. Such behavior is explained through dispersion analysis that  
19 allows to track the emergent multi-domain excitations back to single-domain magnetoelectric (ME)  
20 modes. The latter, scattered by a periodic array of domain walls, are shown to endow the domain-  
21 wall-induced electromagnons with a mixed localized mode and a standing- or propagating-wave  
22 characters. Such features can be exploited to reach strikingly large ME conversion and designing  
23 more reliable and ultrafast ME devices with less energy consumption and using, e.g., local probes.

24

## I. INTRODUCTION

25 Recent observations of magnetoelectric (ME) responses in multiferroics, which charac-  
26 terize cross couplings of electric and magnetic properties, has reawakened the interest of  
27 scientists and engineers in this territory of research, particularly in the last two decades  
28 [1–5]. Such cross couplings open opportunities to, e.g., control electrical polarization by  
29 magnetic field or magnetization by electric field. Switching of polarization by magnetic field  
30 can be employed technologically in the design of memory devices and magnetic field sensors  
31 whereas switching of magnetization by electric field is useful in designing low energy con-  
32 sumption storage devices in which data is written electrically and read magnetically [5–11].  
33 The existence of excitations other than phonons, such as magnons, in these systems provides  
34 more functionalities such as controlling the spin waves by electric field or by optical phonons  
35 [6, 12, 13]. The dynamical ME couplings of magnons and phonons, known as electromagnons,  
36 have also attracted considerable attention due to their role in magnetocapacitance and mag-  
37 netodielectric effects [14–17]. Starting in 2006, experimental reports such as exciting spin  
38 waves by light in  $\text{TbMnO}_3$  [18] and activating magnetic excitations by applying electric fields  
39 in  $\text{YMn}_2\text{O}_5$  and  $\text{TbMn}_2\text{O}_5$  [19] kicked off investigations on the origin and mechanism of elec-  
40 tromagnons. In particular, it was also experimentally shown that adjusting Terahertz pulses  
41 with electromagnons of 0.7 and 1.8 THz in  $\text{TbMnO}_3$  can affect its magnetic structure [20].  
42 In 2008, electromagnons were proposed to be observed for the first time in single crystals

[21, 22] and thin films [23] of bismuth ferrite  $\text{BiFeO}_3$  (BFO). Atomistic methods also predicted electromagnons in antiferromagnetic ferroelectrics [24]. A novel dynamical coupling of magnons with acoustic phonons and optical phonons, coined as electroacoustic magnons, was also suggested in 2019 [25, 26]. Electromagnons can have other benefits. For instance, switching the orientation of domains by applying electric fields on multiferroics is typically of the order of milliseconds [20, 27], although the speed of ferromagnetic or ferroelectric domain reorientation (which is a key in the design of data storage devices) is typically of the order of nanoseconds [20]. In order to improve the operation speed of devices, one can apply high frequency magnetic fields or optical pulses which increase the functionality speed to the order of femtoseconds to picoseconds [28–30] or *coherently excite electromagnons* [31]. Based on the latter possibility, and also to advance fundamental knowledge, it is timely to address a presently unknown issue regarding electromagnons, namely if they can also be preferentially localized within the walls of ferroelectric domains (or near the middle of the domains) rather than “only” equally vibrate in the entire system. If such preferential localizations exist, novel effects can emerge. Examples include new resonances in the magnetoelectric responses and/or a local control of the dynamical conversion between electric and magnetic properties. In order to resolve the aforementioned issues, we performed molecular dynamics (MD) simulations within the GHz-THz regime of applied magnetic fields in BFO materials possessing ferroelectric domain walls. Fourier analysis of temporal evolution of dipole and magnetic moments along with the calculations of quadratic magnetoelectric response of BFO reveals that the existence of domain walls does result in the emergence of *domain-wall-induced electromagnons*, which in turn induce large enhancement of ME response around their resonances. These novel quasi-particles were further found to either be preferentially localized near the domain walls or near the center of the domains (depending on their frequency and direction of propagation of their optical phonon and magnon), as a result of scattering by the periodic array made by the domain walls. Such discoveries have the potential to pave the way for designing original devices. For instance, although the capabilities of magnons as the carriers of information in the field of magnonics is quite promising [32], one of the main challenges is to find a way to control the two-dimensional propagation of the magnons in an energy-efficient fashion, especially in small length scales. A previously proposed approach, which was also realized in experiment recently [33], is to guide the spin-waves in a reconfigurable domain wall as magnonic waveguides. Here, the

75 present work revealing the existence of domain-wall-induced electromagnons strongly sug-  
 76 gests that magnonic circuitry can be utilized by activating, *via electric fields*, the magnons  
 77 associated with such preferentially localized electromagnons. This should allow to design  
 78 novel configurable electronic circuits with much less energy consumption.

79 The article is organized as follows. Section II details the method used here, while results  
 80 are presented and discussed in Section III. Finally, Section IV provides a summary of this  
 81 work.

## 82 II. METHODS

83 An effective Hamiltonian framework developed for bismuth ferrite and detailed in Ref.  
 84 [34] is employed to perform molecular dynamics simulations for the investigation of the tem-  
 85 poral evolution of polarization and magnetization as well as the quadratic magnetoelectric  
 86 response of BFO (which is one of the few materials with magnetoelectric functionalities at  
 87 room temperature, making it a prime candidate for designing novel devices [10, 35–37]) un-  
 88 der the application of magnetic fields with various frequencies from 10 to 1300 GHz. Note  
 89 that the applied time-dependent magnetic field can generate an inhomogeneous electric field  
 90 which we neglected here in order to merely focus on the ME response rather than the polar-  
 91 ization caused by the dielectric response of BFO. In addition, modeling such an electric field  
 92 was not feasible in the simulations because of using periodic boundary conditions in all three  
 93 Cartesian directions. Note also that our molecular dynamics simulations are performed at  
 94 the temperature of 10  $K$  to reduce numerical noises. However, we numerically found that  
 95 conducting them at room temperature leads to similar results albeit with lower numerical  
 96 resolutions for the magnetoelectric coefficients [25].

97 This presently used effective Hamiltonian scheme encompasses three main energy contri-  
 98 butions given by Equation 1 [13, 34, 38]:

$$E^{tot} = E^{FE}(\{\mathbf{u}\}, \{\eta_l\}) + E^{AFD}(\{\mathbf{u}\}, \{\eta_l\}, \{\boldsymbol{\omega}\}) + E^{MAG}(\{\mathbf{m}\}, \{\mathbf{u}\}, \{\eta_l\}, \{\boldsymbol{\omega}\}). \quad (1)$$

99 In Equation 1, local modes  $\{\mathbf{u}\}$  are directly related to local electric dipoles. Strain tensor  
 100  $\{\eta_l\}$  includes both homogeneous  $\{\eta_H\}$  and inhomogeneous  $\{\eta_I\}$  strains. The tiltings of  
 101 oxygen octahedra (also known as antiferrodistortive or AFD motions) are denoted by  $\{\boldsymbol{\omega}\}$ ,  
 102 and the magnetic moments associated with iron ions are denoted by  $\{\mathbf{m}\}$ . Also, in Equation

103 1, the first term includes the energy of local modes and elastic deformations that can be  
 104 written as [39, 40]

$$\begin{aligned}
 E^{FE} = & E^{self}(\{\mathbf{u}\}) + E^{dpl}(\{\mathbf{u}\}) + E^{dpl}(\{\mathbf{u}\}) + E^{short}(\{\mathbf{u}\}) \\
 & + E^{elas}(\{\eta\}) + E^{int}(\{\mathbf{u}\}, \{\eta\}),
 \end{aligned}
 \tag{2}$$

105 in which  $E^{self}$  is the self-energy of local-modes,  $E^{dpl}$  denotes the long-range dipole-dipole  
 106 interaction,  $E^{short}$  is the short-range interaction of soft modes,  $E^{elas}$  denotes the contribution  
 107 of elastic energy, and  $E^{int}$  is the interaction of local modes and strain. [An extensive overview](#)  
 108 [and explanation on the energy terms of Equation 2 is provided in Ref. \[40\].](#)

109 The second term of Equation 1, whose energy is only related to AFD motions and their  
 110 couplings with local modes and strains, is given by

$$\begin{aligned}
 E^{AFD} = & \sum_i [\kappa_A \omega_i^2 + \alpha_A \omega_i^4 + \gamma_A (\omega_{ix}^2 \omega_{iy}^2 + \omega_{iy}^2 \omega_{iz}^2 + \omega_{ix}^2 \omega_{iz}^2)] \\
 & + \sum_{ij} \sum_{\alpha\beta} D_{ij\alpha\beta} \omega_{i\alpha} \omega_{j\beta} \\
 & + \sum_i \sum_{\alpha\beta} C_{i\alpha\beta} \eta_l(i) \omega_{i\alpha} \omega_{i\beta} \\
 & + \sum_{ij} \sum_{\alpha\beta} K_{ij,\alpha\beta} u_{j,\alpha} \omega_{i,\alpha} \omega_{j,\beta} \\
 & + \sum_i \sum_{\alpha\beta\gamma\delta} E_{\alpha\beta\gamma\delta} \omega_{i\alpha} \omega_{i\beta} u_{i\gamma} u_{i\delta},
 \end{aligned}
 \tag{3}$$

111 where indices  $i$  and  $j$  numerate the lattice sites and  $\alpha$ ,  $\gamma$ ,  $\nu$ , and  $\delta$  are the Cartesian  
 112 components. In Equation 3, the first term shows the contribution of self-energy of the tilting  
 113 of the oxygen octahedra while the second term shows the contribution of the short range  
 114 interactions of AFD motions. The third term shows the coupling of the AFD motions with  
 115 strain. The fourth and fifth terms show the contributions of trilinear and biquadratic energies  
 116 coupling the local modes and AFD distortions. More details about AFD energy contributions  
 117 can be found in Ref. [41]. The third term of Equation 1 shows the magnetic moments and  
 118 the coupling of local modes, strain, and antiferrodistortive motions with magnetic moments

119 as given in the following

$$\begin{aligned}
E^{MAG} = & \sum_{ij\alpha\gamma} Q_{ij\alpha\gamma} m_{i\alpha} m_{j\gamma} \\
& + \sum_{ij\alpha\gamma} S_{ij\alpha\gamma} m_{i\alpha} m_{j\gamma} \\
& + \sum_{ij,\alpha\gamma\nu\delta} E_{ij,\alpha\gamma\nu\delta} m_{i\alpha} m_{j\gamma} u_{i\nu} u_{j\delta} \\
& + \sum_{ij,\alpha\gamma\nu\delta} F_{ij,\alpha\gamma\nu\delta} m_{i\alpha} m_{j\gamma} \omega_{i\nu} \omega_{j\delta} \\
& + \sum_{ijl,\alpha\gamma} G_{ijl,\alpha\gamma} \eta_l(i) m_{i\alpha} m_{j\gamma} \\
& + \sum_{ij} L_{ij} (\boldsymbol{\omega}_i - \boldsymbol{\omega}_j) \cdot (\mathbf{m}_i \times \mathbf{m}_j).
\end{aligned} \tag{4}$$

120 In Equation 4, the first term indicates the dipolar interactions of the magnetic moments.  
121 The second term shows the short-range magnetic exchange coupling. The third, fourth, and  
122 fifth terms indicate the contribution of local modes, AFD motions, and strain in magnetic  
123 exchange interaction, respectively. The sixth term shows the contribution of the tilting of  
124 oxygen octahedra through Dzyaloshinskii-Moriya interaction [42–44]. In addition to the  
125 energy contributions discussed above, if external magnetic and/or electric fields are applied,  
126 their contribution to the energy as  $-\sum_i \mathbf{m}_i \cdot \mathbf{H}$  for magnetic field and  $-\sum_i \mathbf{P}_i \cdot \mathbf{E}$  for  
127 electric field should be added to the total energy terms. The electrical polarization,  $\mathbf{P}$ ,  
128 can be computed from its proportionality to the local modes via  $\mathbf{P} = \frac{Z^* \mathbf{u}}{V_0}$  in which  $Z^*$   
129 is Born effective charge obtained from first-principle calculations and its value for BFO is  
130  $Z^* = 5.68 C$  [45], while  $V_0$  is the volume of the unit cell.

131 To predict the dynamical properties of  $BiFeO_3$  within the Effective Hamiltonian frame-  
132 work used here, Newtonian equations of motion are applied for the ionic degrees of freedom  
133 (i.e. local modes, AFD, strains) discussed in Equation 1 where the forces were computed by  
134 taking partial differential of the total energy terms similar to the techniques used in Refs.  
135 [46–48]. Moreover, as demonstrated in Ref. [13], the dynamics of the magnetic moments  
136 are considered through the Landau–Lifshitz–Gilbert (LLG) equation [49] as indicated in the  
137 following:

$$\begin{aligned}
\frac{d\mathbf{m}_i}{dt} = & -\Gamma \mathbf{m}_i \times [\mathbf{B}_{\text{eff}}^i(t) + \mathbf{b}_{\text{fl}}^i(t)] - \Gamma \frac{\lambda}{|\mathbf{m}_i| (1 + \lambda^2)} \mathbf{m}_i \\
& \times \{ \mathbf{m}_i \times [\mathbf{B}_{\text{eff}}^i(t) + \mathbf{b}_{\text{fl}}^i(t)] \}.
\end{aligned} \tag{5}$$

138 Here,  $\mathbf{B}_{\text{eff}}^i$  is the effective magnetic field which acts on the  $i$ th magnetic moment and is  
 139 given by  $\mathbf{B}_{\text{eff}}^i = -\partial E_{\text{tot}}/\partial \mathbf{m}_i$ , while  $\Gamma$  and  $\lambda$  are gyromagnetic and damping coefficients,  
 140 respectively.  $\mathbf{b}_{\text{fl}}^i$  is a fluctuation field which is also acting on the  $i$ th magnetic moment.  
 141 More details on the dynamics of magnetic properties calculations are given in Ref [13].

### 142 III. RESULTS AND DISCUSSION

#### 143 A. Polarization, Magnetization, and Magnetoelectric Coefficient

144 Here and as shown in Figure 1(a), we investigate BFO with two domains separated by  
 145 a  $109^\circ$  domain wall through a periodic  $20 \times 10 \times 10$  supercell (For comparison, Figure 1(b)  
 146 displays a monodomain). We have investigated  $71^\circ$  and  $180^\circ$  domain configurations as well,  
 147 and the results of our analyses are consistent with  $109^\circ$  configuration. However, since  $109^\circ$   
 148 domain walls are the ones that are found most frequently in BFO bulk materials and the  
 149 most seen ferroelastic domain walls in single crystal samples of BFO, the results for  $109^\circ$   
 150 configuration are shown and discussed here [50, 51]. In Figure 1(a), the left half-side along  
 151 the x-axis (which lies along the pseudo-cubic [100] direction), is made of electric dipoles  
 152 being initially along [111] while the right half-side is formed by electric dipoles initially  
 153 lying along  $[\bar{1}\bar{1}\bar{1}]$ . This supercell is subjected to a magnetic field,  $H = H_{dc} + h_{ac} \sin(\omega t)$ ,  
 154 that is applied along the  $[\bar{2}11]$  direction and which is a combination of a  $dc$  field with an  
 155  $ac$  field of  $\omega$  frequency. We chose  $H_{dc} = 245 \text{ T}$  and  $h_{ac} = 61.2 \text{ T}$  in order to get good  
 156 statistics on the quadratic ME coefficients since, for such fields, linear magnetoelectricity  
 157 has a small effect with respect to the quadratic magnetoelectric coefficients in BFO (see  
 158 Refs. [36, 38] and the Supplementary Information of Ref. [26]). However, and as shown  
 159 in the Supplementary Material, the simulations were performed at lower magnetic fields to  
 160 make sure that the observed results are still valid at magnetic fields that can be applied in  
 161 practical applications.

162 Note that, in the entire supercell, the initial magnetization is along the  $[\bar{2}11]$  direction,  
 163 i.e., along which the magnetic field is applied, while the G-type antiferromagnetic vector is  
 164 along the perpendicular  $[01\bar{1}]$  direction. Furthermore,  $\omega$  is fixed during each simulation, but  
 165 is allowed to vary from 10 GHz to 1300 GHz between different computations. The upper  
 166 limit of investigated frequencies is intentionally chosen such as to avoid resonating with the



167  $A_1$  phonon frequencies (known to occur at much higher frequencies of the order of  $\sim 4300$   
 168 and  $\sim 7000$  GHz [25, 52]), but rather to focus on the possibility of having electromagnons  
 169 associated with domain walls and thus occurring at lower frequencies (note that we do see  
 170 these  $A_1$  phonon frequencies in our simulations but do not report them here).

171 Note also that the homogeneous strain has been recently predicted to combine with optical  
 172 phonons and magnons to create a new quasi-particle, coined electroacoustic magnon, that  
 173 can result in the emergence of resonance in the magnetoelectric response [26]. Since we  
 174 are especially interested here in revealing domain-wall-induced electromagnons (i.e., mixing  
 175 of optical vibrations with magnons in a multidomain structure), we perform two kinds  
 176 of MD simulations: one for which the homogeneous strain is clamped (implying that no  
 177 electroacoustic magnon can exist) *versus* another for which such strain is fully relaxed. The  
 178 inhomogeneous strain, on the other hand, is considered in the effective Hamiltonian and can  
 179 vary during the course of all types of simulations conducted here.

180 Note also that, in multiferroics, the electrical polarization under the influence of applied  
 181 electric and magnetic fields can be obtained by differentiating the expansion of the free  
 182 energy with respect to electric field [5]. In the absence of external applied electric fields  
 183 and when neglecting the linear magnetoelectric coefficient, the temporal evolution of the  
 184 polarization as a function of our applied magnetic fields is given by

$$P(t) = P_{(t=0)} + \beta(0, \omega) H_{dc} h_{ac} \sin(\omega t) + \beta(\omega, \omega) \frac{1}{2} h_{ac}^2 \sin^2(\omega t). \quad (6)$$

185 where  $\beta(0, \omega)$ , on which we primarily focus, is the quadratic ME coefficient coupling the  $ac$   
 186 and  $dc$  fields, while  $\beta(\omega, \omega)$  couples the  $ac$  field with itself and generates a second harmonic  
 187 at  $2\omega$ .

188 The real and imaginary parts of  $\beta(0, \omega)$  can thus be obtained by

$$\beta'(0, \omega) = \frac{\frac{2}{\tau} \int_0^\tau (P - P_{(t=0)}) \sin(\omega t) dt}{H_{dc} h_{ac}}, \quad (7)$$

189 and

$$\beta''(0, \omega) = \frac{\frac{2}{\tau} \int_0^\tau (P - P_{(t=0)}) \cos(\omega t) dt}{H_{dc} h_{ac}}, \quad (8)$$

190 in which  $\tau$  is the overall time of the simulation. More details about the derivation of  
 191 equations (7) and (8) are provided within the Supplementary Material.

## B. Frequency Analysis

Let us first consider the case of the aforementioned multidomain structure *when the homogeneous strain is clamped*. During and at the end of the simulation, the overall polarization is along the [100] direction, since the y- and z-components of the dipoles in the left and right domains cancel each other. Furthermore, the direction of the magnetic moments during and at the end of the simulation is found to be along the applied *dc* magnetic field, i.e.,  $[\bar{2}11]$ , in both domains.

We then perform Fourier analysis of the temporal evolution of this electrical polarization and resulting magnetization along different directions (in order to, e.g., reveal the directions of vibration of phonons and magnons that are dynamically coupled to form electromagnons). Note that here we are dealing with two types of frequencies, one being the frequency of applied magnetic field which is denoted by  $\omega$ , while the other is the frequency spectrum that we get as a result of Fourier analyses of the dynamical evolution of the polarization or magnetization under the applied field. For instance, the frequency spectra of the electrical [100]-component of the dipoles (direction of polarization, as well as normal to the ferroelectric domain wall) and the perpendicular, [011]-component, when the frequency of the applied magnetic field,  $\omega$ , is 10 GHz are demonstrated by red solid lines in Figures 2a and 2c, respectively, and up to about 1300 GHz. Apart from the frequency of applied field and its second harmonic at 10 and 20 GHz, two peaks are observed at  $\sim 390$  and  $\sim 1150$  GHz in the spectrum of the [100]-component (Figure 2a). Also a peak is observed at  $\sim 700$  GHz for the [011]-component (Figure 2c).

In addition, the Fourier analyses of the magnetization were performed for the  $[\bar{2}11]$ -component which is also the direction of the magnetic moments and the applied magnetic field (Figure 2b) as well as the  $[01\bar{1}]$ -component which is also a direction that is perpendicular to both polarization and magnetization (Figure 2d). Since the peaks at  $\sim 390$  GHz and  $\sim 1150$  GHz are present in the Fourier analyses of both [100]-component of polarization and  $[\bar{2}11]$ -component of magnetization, these peaks represent *electromagnons* for which the optical phonon has a component of its vibration along the direction that is perpendicular to the domain wall and the magnon has a component of its vibration along the magnetization. (It should be noted that, we found such electromagnons for the  $71^\circ$  domain configuration at  $\sim 455$  GHz and  $\sim 1390$  GHz. Also, for the  $180^\circ$  domain configuration, such electromagnons

223 are found to be at 240 GHz and 1430 GHz). Similarly, the peaks at  $\sim 700$  GHz seen in Figs  
 224 2c and 2d characterize an electromagnon made of an optical phonon that has a vibration  
 225 direction with a component lying along the  $[011]$  direction and of a magnon for which the  
 226 vibration has a finite component along  $[01\bar{1}]$  (note that  $[011]$  and  $[01\bar{1}]$  are both lying in the  
 227 plane of the domain wall but are perpendicular to each other). Interestingly, and as verified  
 228 by black solid lines in Figures 2a to 2d, these three peaks disappear when the simulations  
 229 are performed for the case of monodomain structure (whether the homogeneous strain is  
 230 clamped or unclamped). In other words, one can conclude that the 390, 1150, and 700 GHz  
 231 modes are *domain-wall-induced* electromagnons (to be denoted as DWI electromagnons in  
 232 the following). Such observations are also consistent with previous findings that vibrations  
 233 of the order of 360, 700 and  $\sim 1200$ -1800 GHz caused by domain wall motions were pre-  
 234 dicted for the case of BFO adopting domain structures [50, 53] (note that other domain wall  
 235 activities, but with lower frequencies, were also reported in Refs. [54, 55] but the limitation  
 236 of molecular dynamics methods below the range of few GHz prevents us from determining  
 237 them).

238 Figures 2a, 2b, 2c, and, 2d also report the case of a multidomain but *for unclamped homoge-*  
 239 *neous strain*, which is represented by dashed blue lines. In this latter case, three additional  
 240 peaks are observed at 70, 100 and 270 GHz with respect to the case of clamped multidomain,  
 241 for both the Fourier transform of the temporal evolution of the polarization and magnetiza-  
 242 tion. These three peaks, therefore, indicate that strain can mix with optical lattice vibrations  
 243 and magnons to produce new particles – which is in-line with the recent prediction of the  
 244 so-called electroacoustic magnons for unclamped monodomain in Ref. [25]. Note that these  
 245 electroacoustic magnons at 70 and 270 GHz in our multidomain involve vibration of the  
 246 polarization along the normal of the domain wall (see Fig. 2a) while that at 100 GHz is  
 247 better seen in the oscillation of the electric dipoles perpendicularly to that normal (cf Fig.  
 248 2c). Moreover, the magnon associated with these electroacoustic magnons at 70, 100 and  
 249 270 GHz have vibrations along both  $[\bar{2}11]$  (that are stronger) and  $[01\bar{1}]$  (that are weaker),  
 250 as demonstrated by Figures 2b and 2d.

### 251 C. Magnetolectric Response

252 Let us from now on focus on results obtained *for the case of unclamped homogeneous strain*  
 253 in the multidomain structure, since we now know the origins of all the peaks appearing  
 254 in Figure 2. The real and imaginary parts of the quadratic magnetolectric coefficient,  
 255  $\beta(0, \omega)$ , for polarization lying along the [100] and [011] directions, are then computed using  
 256 Equations (7) and (8) at each frequency of applied magnetic field from 10 to 1300 GHz in  
 257 that case. They are shown in Figures 3a and 3b, respectively. The calculated values are  
 258 in agreement with experimental measurements of  $\beta$  of bulk BFO at small frequencies. For  
 259 instance, the obtained value for the real part of  $\beta(0, \omega)$  along the [100] direction by our MD  
 260 simulations when the frequency of applied magnetic field is 20 GHz and the homogeneous  
 261 strain is unclamped, is  $2.457 \times 10^{-8} C/m^2T^2 = 0.388 \times 10^{-19} s/A$  which remarkably agrees  
 262 with the observation of  $\beta_{311} = 0.3 \times 10^{-19} s/A$  reported in Reference [56] for the static case.  
 263 Also, in measurements that were performed in high magnetic fields [57], the quadratic ME  
 264 coefficient was found to be  $\beta_{122} = \beta_{212} = \beta_{221} = -\beta_{111} = -5 \times 10^{-9} C/m^2T^2$  which is in  
 265 reasonable agreement with the value of  $-1.004 \times 10^{-9} C/m^2T^2$  that we have computed along  
 266 the [011] direction at  $\omega=20$  GHz. The ME coefficients exhibit resonances when the frequency  
 267 of applied magnetic field,  $\omega$ , approaches the frequency of the electroacoustic-magnon-like  
 268 particles mentioned above, that are 70, 100 and 270 GHz here, as previously found for the  
 269 case of a monodomain, for which electroacoustic magnons have resonant frequencies at 90  
 270 and 267 GHz [25, 26].

271 Moreover, another important novelty of the present work is that resonances also happen  
 272 when  $\omega$  reaches the frequency of the three domain-wall-induced electromagnons. For in-  
 273 stance, along the [011] direction, a nicely seen resonance takes place at  $\omega=700$  GHz, while,  
 274 along the [100] direction, one resonance is rather sharp at 390 GHz while the other one  
 275 around 1150 GHz is broader and even seems to be made of several peaks – which is rem-  
 276 iniscent of the broad response found in Ref. [53] around these frequencies for the domain  
 277 wall motions. These results are also consistent with the dielectric and domain-wall-related  
 278 modes  $A$  and  $B$  reported in Ref. [50] for which mode  $A$  around  $12 \text{ cm}^{-1} \simeq 360 \text{ GHz}$  is  
 279 sharp while mode  $B$  around  $50 \text{ cm}^{-1} \simeq 1500 \text{ GHz}$  is broader. Our DWI electromagnons  
 280 therefore provide a path to engineer devices based on the functionality of the domain walls.  
 281 Although domain walls have already been employed in spintronics and for designing novel

282 devices [58–60], their presently discovered role in optimizing ME responses make them also  
 283 fascinating for magnetoelectric-based devices. As a matter of fact, our results show that one  
 284 can tune the frequency of the applied magnetic field with the frequency of the domain wall  
 285 vibrations (DWI electromagnons) to maximize the ME response.

#### 286 **D. Degree of localization of the domain-wall-induced electromagnons**

287 In order to investigate the degree of localization that these DWI electromagnons possess,  
 288 a layer-by-layer analysis is performed at different planes that are parallel to the domain wall.  
 289 As the dimension of the supercell is  $20 \times 10 \times 10$ , each  $10 \times 10$  cross section of the supercell  
 290 along the [100] direction is defined as a layer for which the average of magnetization and  
 291 polarization can be computed from the MD simulation results. Also, the quadratic ME  
 292 coefficient of each layer can be obtained via equations (7) and (8) but for which the overall  
 293 polarization is replaced by the average polarization of each layer. The layers are indicated  
 294 by their plane numbers, with the planes 10 and 20 corresponding to the domain wall layers  
 295 whereas planes 5 and 15 correspond to the center of each domain. Since the magnetoelectric  
 296 coefficients  $\beta(0, \omega)$  are calculated at each frequency of applied magnetic field for frequencies  
 297 up to 1300 GHz, in each plane that is parallel to the domain wall, the absolute value of the  
 298 real part of magnetoelectric coefficient,  $|Re(\beta(0, \omega))|$  (which is related to real-space location  
 299 of optical phonons) is used to investigate the preferential location of the optical phonons.  
 300 On the other hand, for each frequency of applied magnetic field, the Fourier analysis of  
 301 magnetic moments provides a spectrum of the frequencies that are present in the vibration  
 302 of the magnetic moments. Therefore, the Fourier intensity of the magnetization which is  
 303 related to real-space location of magnons is used to investigate the preferential location of  
 304 magnons. Here we used the Fourier analyses when the frequency of applied magnetic field  
 305 is 10 GHz.

306 Figures 4a and 4b provide an example of the results on such analysis for the optical  
 307 phonon (Figure 4a) and magnon (Figure 4b) associated with the frequency of 700 GHz.  
 308 One can see that the maximum value of the resonance peak inside the domain (plane 5),  
 309 which is  $1.732 \times 10^{-8} C/m^2T^2$ , jumps to  $4.393 \times 10^{-8} C/m^2T^2$  at the domain wall (plane 10)  
 310 showing that the ME coefficient is increased by 154%. Such comparison clarifies that not  
 311 only the ME coefficient exhibits a resonance when the frequency of applied magnetic field is

312 700 GHz, but also the resonance is intensified at the domain walls. Furthermore, Figure 4b  
 313 compares the intensity of Fourier analyses peaks around 700 GHz for magnetization along  
 314 the  $[01\bar{1}]$  direction in each layer. The Fourier intensity of vibrations of magnetization at  
 315  $\omega=700$  GHz is stronger at the domain wall. Consequently, one can conclude that the DWI  
 316 electromagnon at  $\omega=700$  GHz can be seen as waves that adopt maximum at the domain  
 317 wall, that is both the optical phonon and magnon forming such electromagnon preferen-  
 318 tially localize at this ferroelectric domain wall. Such domain-wall-induced electromagnon's  
 319 wave behavior and preferential localization are also found for the frequency of 1150 GHz  
 320 (but for optical phonon vibrating along  $[100]$  and magnons oscillating along  $[\bar{2}11]$ ). As a  
 321 matter of fact and as demonstrated in Figures 5(a) and (b), both the optical phonon and  
 322 magnon of the domain-wall-induced electromagnon at 1150 GHz adopt wave-like behavior  
 323 with maxima occurring in the vicinity of the domain walls (near plane 10). On the other  
 324 hand, the DWI electromagnon having a resonant frequency of 390 GHz, while still possess-  
 325 ing wave-like behavior, prefers to possess maxima occurring, both for its optical phonon and  
 326 magnon, *near the middle of the domains* (near planes 5 and 15) rather than at the domain  
 327 wall, as demonstrated in Figures 6a and 6b. Note that the Supplementary Material also  
 328 reports information about localization/delocalization of the electroacoustic magnons and  
 329 some results on inhomogeneous strain analysis.

### 330 E. The origin of the domain-wall-induced electromagnons

331 To have a clear understanding of the origin of the 390 GHz, 700 GHz and 1150 GHz  
 332 electromagnons induced by the domain structure, we have analyzed the spectral energy  
 333 density (SED) associated with local dipoles ( $\Phi_P$ ) and inhomogeneous stain ( $\Phi_\eta$ ) when the  
 334 homogeneous strain was unclamped and for a  $40\times 10\times 10$  supercell. In order to conserve the  
 335 periodicity of the domain structure, the supercell is split into four alternating domains of  
 336 equal width. Note that a larger supercell (i.e.  $40\times 10\times 10$  as compared to  $20\times 10\times 10$ ) is used  
 337 to increase the wave-vector  $q$  resolution. Note also that  $\Phi_X$ , with  $X=P$  or  $\eta$ , describes the  
 338 wave-vector  $\mathbf{q}$  and frequency  $\nu$  resolved power of the kinetic energy spectrum for the vector  
 339 degrees of freedom  $X$ . It is computed [61] as

$$\Phi_X(\mathbf{q}) = \frac{1}{N\tau} \sum_{\alpha=x,y,z} \left| \dot{X}_{\mathbf{q},\nu}^\alpha \right|^2, \quad (9)$$

340 where  $\dot{X}_{\mathbf{q},\nu}^\alpha$  denotes the Fast Fourier Transform coefficient of the  $\alpha$  component of the velocity  
 341  $\dot{X}^\alpha$ .  $N$  and  $\tau$  denote the total number of unit cells and the molecular dynamics trajectory  
 342 time, respectively. The poles of  $\Phi_P$  provide the spectrum of excitations independently of  
 343 the mode's polarization vector. Specifically,  $\Phi_P$  and  $\Phi_\eta$  can be used to obtain dispersions of  
 344 optical and acoustic phonons, respectively.

345 Practically, we use a single 0.5 ns molecular dynamics trajectory computed for this  $N =$   
 346  $40 \times 10 \times 10$  supercell. The integration time step is taken to be equal to 0.5 fs and the first  
 347 10,000 steps of the trajectory are not taken into consideration. The velocities are sampled  
 348 each 10 MD steps for a subsequent Fast Fourier transforms to the wave-vector and frequency  
 349 domain.

350 Figure 7a and 7c shows the computed low-frequency spectra of polar excitations along  
 351 the [100] pseudo-cubic direction (i.e., different panels on the left/right side correspond to  
 352 different q-points along that direction) for mono- and multi-domain states, respectively. The  
 353 spectrum for the mono-domain configuration (panel a of Fig. 7) clearly shows the dispersion  
 354 of three electromagnon branches labeled (1)-(3). From the analysis of  $\Phi_\eta$ , we also find that  
 355 these branches follow the dispersion curves of acoustic phonons (not shown here). Branches  
 356 (1) and (2) match the two transverse acoustic (TA) modes, while the third branch is mixed  
 357 with the longitudinal acoustic (LA) mode.

358 Interestingly, the three described monodomain branches can be also clearly seen in the  
 359 spectrum of the multidomain state (see panel c of Fig. 7). However, the multidomain  
 360 spectrum additionally features multiple “satellite” peaks not present in the monodomain  
 361 case (panel a of Fig. 7). These features most likely stem from the elastic scattering of the  
 362 three mono-domain electromagnons by a periodic and static array of domain walls. In such  
 363 hypothetical scenario, a single scattering event would conserve the mode frequency and lead  
 364 to a shift of its momentum  $q_x$  by  $\pm\Delta q_x$ . The possible shifts

$$\Delta q_x = \frac{2}{20} \frac{\pi}{a_0}, \frac{6}{20} \frac{\pi}{a_0}, \frac{10}{20} \frac{\pi}{a_0} \quad (10)$$

365 correspond to the dominant Fourier components of the local mode distribution, or, in other  
 366 words, are determined by the periodicity of the domain structure. Here  $a_0$  indicates the  
 367 5-atom lattice constant.

368 The simplest single scattering mechanism described above allows to explain the appear-  
 369 ance of the predicted domain-wall-induced electromagnons at  $q_x = 0$ . Namely, the emergent

370 zone-center excitations at 390 GHz and 700 GHz can be matched with monodomain modes  
 371 (1) and (3) at  $q_x = \frac{2}{20} \frac{\pi}{a_0}$  that are scattered by  $\Delta q_x = -\frac{2}{20} \frac{\pi}{a_0}$  (see panels a and b of Fig. 8),  
 372 while the homogeneous 1150 GHz mode stems from scattering of mode (1) at  $q_x = \frac{6}{20} \frac{\pi}{a_0}$  by  
 373  $\Delta q_x = -\frac{6}{20} \frac{\pi}{a_0}$  (see panels a and c of Fig. 8).

374 Such hypothesis about the origin of the domain-wall-induced electromagnons is fur-  
 375 ther supported by visualizing the local mode vibrations at  $\nu_0 = 390$  GHz, 700 GHz and  
 376 1150 GHz. To perform this analysis, we first note the deviation of the average local mode  
 377 value  $\delta \mathbf{u}(x, t) = \mathbf{u}(x, t) - \langle \mathbf{u}(x) \rangle$  within each  $x$ -layer of the supercell and at each MD step  $t$   
 378 from its time average  $\langle \mathbf{u}(x) \rangle$ . Then, we perform the time-frequency Fourier transformation  
 379  $\delta \mathbf{u}(x, t) \rightarrow \delta \mathbf{u}(x, \nu)$  that allows us to look at how the layer-averaged local modes change  
 380 along the [100] direction and only at the frequencies of interest (i.e., at these  $\nu_0$ ). We per-  
 381 form the described procedure using the generated MD trajectories for the multidomain case  
 382 which technically corresponds to isolating the excitations pattern at a specific frequency  
 383 in Figure 7c. Figure 9 shows how the resulting complex amplitudes  $\delta u_\alpha(x, \nu_0)$  and phases  
 384  $\theta_\alpha = \arg(\delta \mathbf{u}_\alpha(x, \nu_0))$  change with  $x$  for each Cartesian component  $\alpha$  of the local modes.

385 As expected from the scattering picture, the amplitudes of local modes displacements at  
 386  $\nu_0 = 390$  GHz (Fig. 9a) and  $\nu_0 = 700$  GHz (Fig. 9b) have a pronounced  $q_x = \frac{2}{20} \frac{\pi}{a_0}$  character  
 387 with half of the wave period falling within each of the domains (Figure 7b). At the same  
 388 time, and as also consistent with Figure 8c, the amplitudes  $\delta u_\alpha(x, \nu_0)$  at  $\nu_0 = 1150$  GHz  
 389 (see Figure 9c) have a different, three half-period, character rather described by  $q_x = \frac{6}{20} \frac{\pi}{a_0}$   
 390 (Figure 7b). This latter periodicity is more clearly visible in the dependence of the phase  
 391 on  $x$  at  $\nu_0 = 1150$  GHz (see Figure 9f).

392 It is also interesting to note the markedly distinct behavior of the phase plots at  
 393  $\nu_0 = 390$  GHz and  $\nu_0 = 1150$  GHz from the complex phase distribution at  $\nu_0 = 700$  GHz.  
 394 Indeed, the two former feature a constant (flat) phase  $\theta_\alpha(x)$  dependencies on  $x$  within each  
 395 domain (Figures 9d and f). Such distribution along with a spatially modulated amplitudes  
 396 (Figures 9a and c) are unique signatures of standing waves. Notably, the standing-wave  
 397 character (confinement) of these modes also goes in-line with the TA nature of the original  
 398 monodomain branch (1) giving rise to these modes. Indeed, similar situations were pre-  
 399 viously reported in references [62, 63] describing the confinement of TA acoustic phonons  
 400 in semiconductor superlattices. In contrast, the  $\nu_0 = 700$  GHz vibration pattern rather cor-  
 401 responds to a propagating wave as the latter typically yield a linear phase dependence on



402 the coordinate (see Figure 9 e). This observation also goes in-line with our prediction of  
 403 the common origin of the  $\nu_0 = 390$  GHz and  $\nu_0 = 1150$  GHz electromagnons distinct from  
 404 that of the  $\nu_0 = 700$  GHz domain-wall-induced mode. Finally, from Figures 9 it can be  
 405 further noted that for all of the considered frequencies the vibration patterns are neither the  
 406 classical standing nor classical propagating waves. Indeed, the amplitude plots in Figures 9  
 407 clearly indicate that all modes are mixed with Gamma point vibrations while the amplitude  
 408 deviations at the domain walls indicate the presence of domain-wall localized modes. More-  
 409 over, the phase velocity of the propagating electromagnon at  $\nu_0 = 700$  GHz clearly increases  
 410 upon approaching the domain walls (Figure 9e) while, at the same time, its amplitude  
 411 experiences a drop. Such change of the phase velocity can be equivalently described as a  
 412 mixing of the propagating mode with a domain-wall localized mode and a standing wave  
 413 at  $q_x = \frac{2}{20} \frac{\pi}{a_0}$ . All of the described deviations are due to the aforementioned scattering  
 414 which couples phonons with wavevectors differing by the multiples of  $\frac{2}{20} \frac{\pi}{a_0}$  due to which all  
 415 of the three modes have a mixed character. To complete the picture, we summarize the  
 416 information presented in Figure 9 by plotting the instantaneous snapshots of the calculated  
 417 profiles of dipole vibrations at  $\nu_0 = 390$  GHz, 700 GHz and 1150 GHz in Figure 10.

418 Based on the gathered insights, we now fit (as an example) the values of the Fourier  
 419 intensity peaks of ME coefficient,  $\beta(0, \omega)$ , along the [100] direction and at 390 GHz by a  
 420 function of the form

$$y = A + C|\sin(q(x - x_0))| \quad (11)$$

421 where  $q = \frac{2}{20} \frac{\pi}{a_0}$  is the scattering vector for that frequency,  $A$  is the amplitude of the zone-  
 422 center mode and  $C$  can be seen as an x-component amplitude of the confined electromagnon  
 423 at  $q$ . One can clearly see that such function fits well the data of Fig. 6a, which confirms  
 424 our proposed concept of scattering. Similarly, the values of the Fourier intensity peaks of  
 425 magnetization along the  $[\bar{2}11]$  direction at 390 GHz were fitted by a function of the form

$$y = A + C'|\sin(q(x - x_0))| + D'\sin(q(x - x_0)) \quad (12)$$

426 where  $q$  is still equal to  $\frac{2}{20} \frac{\pi}{a_0}$ ,  $C'$  is related to the x-component contribution of the elec-  
 427 tromagnon as in Eq.(11), while  $D'$  originates from its y- and z-components. Once again,  
 428 this function fits well the data of Fig. 6b, which is another confirmation that scattering is  
 429 the main source of the domain-wall-induced electromagnons. It should be noted that the  
 430 difference between the data and the fit at domain walls comes from the modes localized on

431 the domain walls.

#### 432 **IV. SUMMARY**

433 In summary, we report here the existence and explain the origin of domain-wall-induced  
434 electromagnons, and discover that they enhance the magnetoelectric response of the mate-  
435 rial to the application of external magnetic fields. Obtaining such results for bisumth ferrite  
436 not only implies that ME enhancement can be achieved at room temperature, but also  
437 infers that such enhancement can be generalized to other multiferroics possessing multido-  
438 mains. Interestingly, the optical phonon and magnons forming such domain-wall-induced  
439 electromagnons behave as waves for which the maxima jointly occur in some specific parts  
440 of the multidomain, namely near the domain walls for the 700 and 1150 GHz frequencies  
441 *versus* near the middle of each domain for the 390 GHz frequency. The presently discov-  
442 ered domain-wall-induced electromagnons may thus be of some advantages for, e.g., the  
443 design of (i) novel ultra-fast energy-efficient data storage devices via local probes and (ii)  
444 and of electrically-driven configurable magnonic circuits taking advantage of the spatial  
445 preferential localization of both the phonons and magnons making the domain-wall-induced  
446 electromagnons.

#### 447 **ACKNOWLEDGEMENTS**

448 The authors are thankful to the DARPA Grant No. HR0011-15-2-0038 (under the  
449 MATRIX program). S. Prosandeev also thanks ONR Grants No. N00014-17-1-2818 and  
450 N00014-21-1-2086. B.X. further acknowledges the financial support from National Natu-  
451 ral Science Foundation of China under Grant No. 12074277, the startup fund from Soo-  
452 chow University, and the support from Priority Academic Program Development (PAPD)  
453 of Jiangsu Higher Education Institutions. S. Prokhorenko and Y.N. thank DARPA Grant  
454 No. HR0011727183-D18AP00010 (under the TEE Program). The authors are also thankful  
455 for the support of MRI Grant No. 0722625 from NSF, ONR Grant No. N00014-15-1-2881  
456 (DURIP), as well as a Challenge grant from the Department of Defense, and also acknowl-

- [1] Y. Tokura and S. Seki, *Advanced materials* **22**, 1554 (2010).
- [2] S.-W. Cheong and M. Mostovoy, *Nature materials* **6**, 13 (2007).
- [3] T. Kimura, T. Goto, H. Shintani, K. Ishizaka, T.-h. Arima, and Y. Tokura, *nature* **426**, 55 (2003).
- [4] Y. Takahashi, R. Shimano, Y. Kaneko, H. Murakawa, and Y. Tokura, *Nature Physics* **8**, 121 (2012).
- [5] M. Fiebig, *Journal of physics D: applied physics* **38**, R123 (2005).
- [6] A. Kumar, J. Scott, and R. S. Katiyar, *Applied physics letters* **99**, 062504 (2011).
- [7] J. Wang, J. Neaton, H. Zheng, V. Nagarajan, S. Ogale, B. Liu, D. Viehland, V. Vaithyanathan, D. Schlom, U. Waghmare, *et al.*, *science* **299**, 1719 (2003).
- [8] W. Eerenstein, N. Mathur, and J. F. Scott, *nature* **442**, 759 (2006).
- [9] D. Lebeugle, D. Colson, A. Forget, M. Viret, A. Bataille, and A. Gukasov, *Physical review letters* **100**, 227602 (2008).
- [10] G. Catalan and J. F. Scott, *Advanced materials* **21**, 2463 (2009).
- [11] D. Khomskii, *Physics* **2**, 20 (2009).
- [12] E. Albisetti, S. Tacchi, R. Silvani, G. Scaramuzzi, S. Finizio, S. Wintz, C. Rinaldi, M. Cantoni, J. Raabe, G. Carlotti, *et al.*, *Advanced Materials* , 1906439 (2020).
- [13] D. Wang, J. Weerasinghe, and L. Bellaiche, *Physical review letters* **109**, 067203 (2012).
- [14] Y. Zhang, Y. Zhang, Q. Guo, D. Zhang, S. Zheng, M. Feng, X. Zhong, C. Tan, Z. Lu, J. Wang, *et al.*, *Physical Chemistry Chemical Physics* **21**, 21381 (2019).
- [15] R. V. Aguilar, A. Sushkov, C. Zhang, Y. J. Choi, S.-W. Cheong, and H. Drew, *Physical Review B* **76**, 060404 (2007).
- [16] R. de Sousa and J. E. Moore, *Physical Review B* **77**, 012406 (2008).
- [17] Z. Chen, M. Schmidt, Z. Wang, F. Mayr, J. Deisenhofer, A. Mukhin, A. Balbashov, and A. Loidl, *Physical Review B* **93**, 134406 (2016).
- [18] A. Pimenov, A. Mukhin, V. Y. Ivanov, V. Travkin, A. Balbashov, and A. Loidl, *Nature physics* **2**, 97 (2006).

- [19] A. Sushkov, R. V. Aguilar, S. Park, S.-W. Cheong, and H. Drew, Physical review letters **98**, 027202 (2007).
- [20] T. Kubacka, J. A. Johnson, M. C. Hoffmann, C. Vicario, S. De Jong, P. Beaud, S. Grübel, S.-W. Huang, L. Huber, L. Patthey, *et al.*, Science **343**, 1333 (2014).
- [21] M. Cazayous, Y. Gallais, A. Sacuto, R. De Sousa, D. Lebeugle, and D. Colson, Physical review letters **101**, 037601 (2008).
- [22] M. K. Singh, R. S. Katiyar, and J. Scott, Journal of Physics: Condensed Matter **20**, 252203 (2008).
- [23] A. Kumar, N. Murari, and R. Katiyar, Applied Physics Letters **92**, 152907 (2008).
- [24] C.-M. Chang, B. Mani, S. Lisenkov, and I. Ponomareva, Ferroelectrics **494**, 68 (2016).
- [25] S. O. Sayedaghaee, B. Xu, S. Prosandeev, C. Paillard, and L. Bellaiche, Physical review letters **122**, 097601 (2019).
- [26] S. O. Sayedaghaee, C. Paillard, S. Prosandeev, B. Xu, and L. Bellaiche, npj Computational Materials **6**, 1 (2020).
- [27] T. Hoffmann, P. Thielen, P. Becker, L. Bohatý, and M. Fiebig, Physical Review B **84**, 184404 (2011).
- [28] S. Johnson, R. De Souza, U. Staub, P. Beaud, E. Möhr-Vorobeva, G. Ingold, A. Caviezel, V. Scagnoli, W. Schlotter, J. Turner, *et al.*, Physical review letters **108**, 037203 (2012).
- [29] I. Handayani, R. Tobey, J. Janusonis, D. Mazurenko, N. Mufti, A. Nugroho, M. Tjia, T. Palstra, and P. Van Loosdrecht, Journal of physics: Condensed matter **25**, 116007 (2013).
- [30] D. S. Rana, I. Kawayama, K. Mavani, K. Takahashi, H. Murakami, and M. Tonouchi, Advanced Materials **21**, 2881 (2009).
- [31] M. Mochizuki and N. Nagaosa, Physical review letters **105**, 147202 (2010).
- [32] A. V. Chumak, V. I. Vasyuchka, A. A. Serga, and B. Hillebrands, Nature Physics **11**, 453 (2015).
- [33] K. Wagner, A. Kákay, K. Schultheiss, A. Henschke, T. Sebastian, and H. Schultheiss, Nature nanotechnology **11**, 432 (2016).
- [34] S. Prosandeev, D. Wang, W. Ren, J. Íñiguez, and L. Bellaiche, Advanced Functional Materials **23**, 234 (2013).
- [35] D. Edwards, N. Browne, K. M. Holsgrove, A. B. Naden, S. O. Sayedaghaee, B. Xu, S. Prosandeev, D. Wang, D. Mazumdar, M. Duchamp, *et al.*, Nanoscale **10**, 17629 (2018).

- [36] S. Lisenkov, I. A. Kornev, and L. Bellaiche, *Physical Review B* **79**, 012101 (2009).
- [37] A. Apostolov, I. Apostolova, S. Trimper, and J. Wesselinowa, *physica status solidi (b)* **254**, 1600433 (2017).
- [38] I. A. Kornev, S. Lisenkov, R. Haumont, B. Dkhil, and L. Bellaiche, *Physical review letters* **99**, 227602 (2007).
- [39] W. Zhong, D. Vanderbilt, and K. Rabe, *Physical Review Letters* **73**, 1861 (1994).
- [40] W. Zhong, D. Vanderbilt, and K. Rabe, *Physical Review B* **52**, 6301 (1995).
- [41] I. A. Kornev, L. Bellaiche, P.-E. Janolin, B. Dkhil, and E. Suard, *Physical review letters* **97**, 157601 (2006).
- [42] B. Xu, B. Dupé, C. Xu, H. Xiang, and L. Bellaiche, *Physical Review B* **98**, 184420 (2018).
- [43] H. Katsura, N. Nagaosa, and A. V. Balatsky, *Physical review letters* **95**, 057205 (2005).
- [44] A. Raeliarijaona, S. Singh, H. Fu, and L. Bellaiche, *Physical review letters* **110**, 137205 (2013).
- [45] D. Rahmedov, Ph. D. Thesis (2014).
- [46] I. Ponomareva, L. Bellaiche, T. Ostapchuk, J. Hlinka, and J. Petzelt, *Physical Review B* **77**, 012102 (2008).
- [47] D. Wang, J. Weerasinghe, L. Bellaiche, and J. Hlinka, *Physical Review B* **83**, 020301 (2011).
- [48] D. Wang, E. Buixaderas, J. Íñiguez, J. Weerasinghe, H. Wang, and L. Bellaiche, *Physical Review Letters* **107**, 175502 (2011).
- [49] J. L. García-Palacios and F. J. Lázaro, *Physical Review B* **58**, 14937 (1998).
- [50] J. Hlinka, M. Paściak, S. Körbel, and P. Marton, *Physical Review Letters* **119**, 057604 (2017).
- [51] F. Borodavka, J. Pokorny, and J. Hlinka, *Phase Transitions* **89**, 746 (2016).
- [52] H. Fukumura, S. Matsui, H. Harima, T. Takahashi, T. Itoh, K. Kisoda, M. Tamada, Y. Noguchi, and M. Miyayama, *Journal of Physics: Condensed Matter* **19**, 365224 (2007).
- [53] S. Prosandeev, Y. Yang, C. Paillard, and L. Bellaiche, *npj Computational Materials* **4**, 1 (2018).
- [54] P. Chen, L. Ponet, K. Lai, R. Cingolani, and S. Artyukhin, *npj Computational Materials* **6**, 1 (2020).
- [55] Y.-L. Huang, L. Zheng, P. Chen, X. Cheng, S.-L. Hsu, T. Yang, X. Wu, L. Ponet, R. Ramesh, L.-Q. Chen, *et al.*, *Advanced Materials* **32**, 1905132 (2020).
- [56] C. Tabares-Munoz, J.-P. Rivera, A. Bezingses, A. Monnier, and H. Schmid, *Japanese Journal of Applied Physics* **24**, 1051 (1985).

- [57] Y. F. Popov, A. Kadomtseva, S. Krotov, D. Belov, G. Vorob'ev, P. Makhov, and A. Zvezdin, *Low Temperature Physics* **27**, 478 (2001).
- [58] K.-J. Kim, S. K. Kim, Y. Hirata, S.-H. Oh, T. Tono, D.-H. Kim, T. Okuno, W. S. Ham, S. Kim, G. Go, *et al.*, *Nature materials* **16**, 1187 (2017).
- [59] O. Gomonay, T. Jungwirth, and J. Sinova, *Physical review letters* **117**, 017202 (2016).
- [60] H. Awano, *Journal of Magnetism and Magnetic Materials* **383**, 50 (2015).
- [61] J. A. Thomas, J. E. Turney, R. M. Iutzi, C. H. Amon, and A. J. H. McGaughey, *Phys. Rev. B* **81**, 081411 (2010).
- [62] C. Colvard, T. A. Gant, M. V. Klein, R. Merlin, R. Fischer, H. Morkoc, and A. C. Gossard, *Phys. Rev. B* **31**, 2080 (1985).
- [63] M. V. Klein, *IEEE Journal of Quantum Electronics* **22**, 1760 (1986).

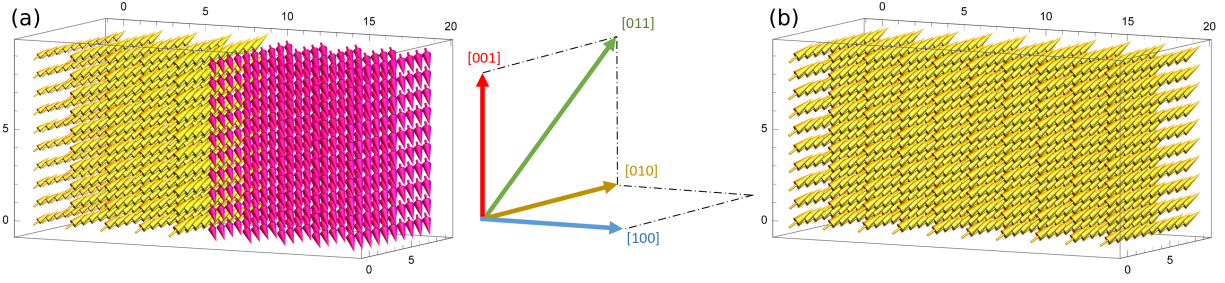


FIG. 1: (Color online) Schematic representation of the electric dipole moments for a  $20 \times 10 \times 10$  supercell of  $\text{BiFeO}_3$

- (a) a multidomain structure in which electric dipole moments are initially along the  $[111]$  direction in the first (left) domain and along  $[\bar{1}\bar{1}\bar{1}]$  in the second (right) domain; (b) a monodomain structure in which all electric dipole moments are along the pseudocubic  $[111]$  direction

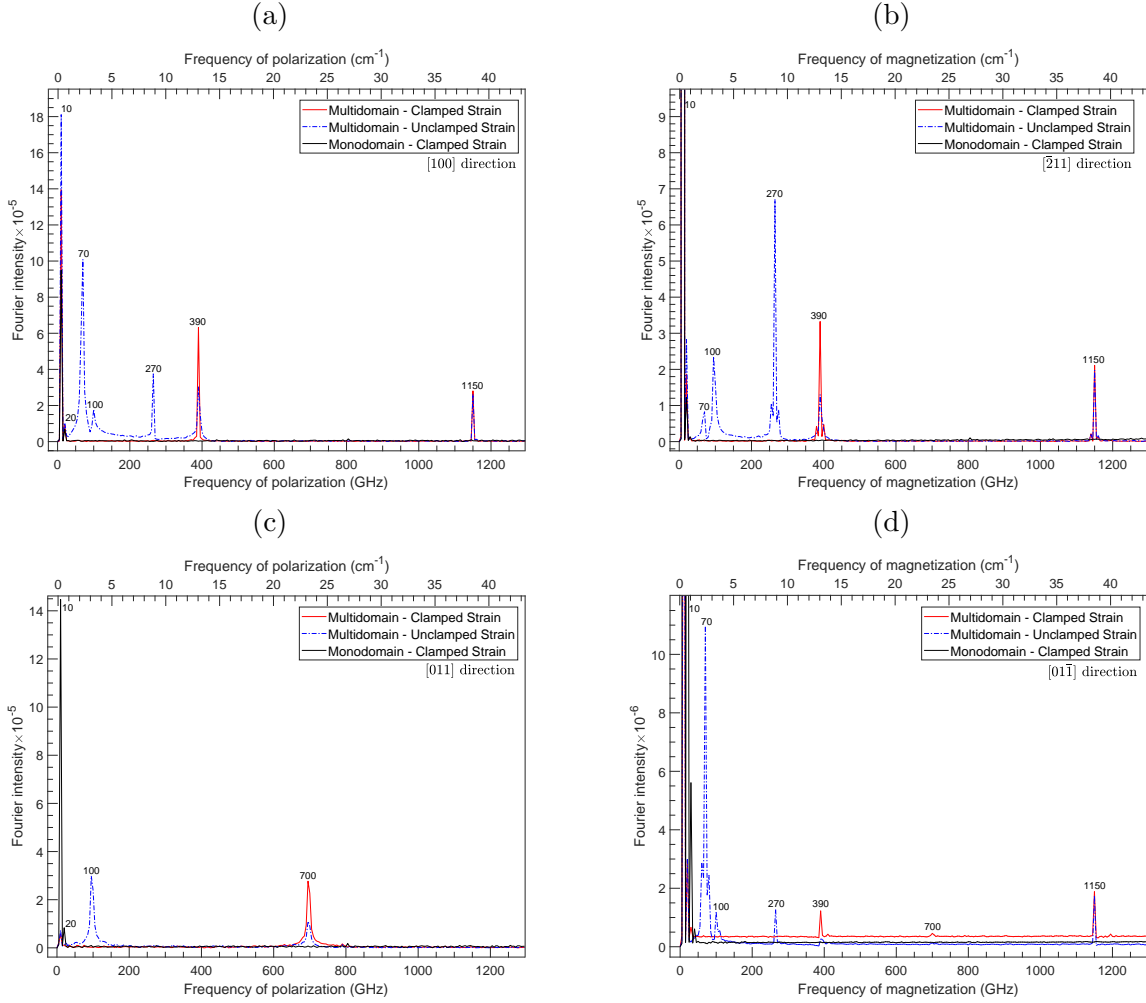


FIG. 2: (Color online) The Fourier analyses

The Fourier analyses of the polarization (panel a is for polarization along the [100] direction while panel c is for polarization along the [011] direction) and magnetization (panel b is for magnetization along the [211] direction while panel d is for magnetization along the [011̄] direction) for the case of monodomain when the strain is unclamped (black) and for the case of multidomain when the homogeneous strain is unclamped (blue) and clamped (red). Here, the frequency of the applied magnetic field is 10 GHz. Note the change of vertical scale between

Panels (b) and (d)



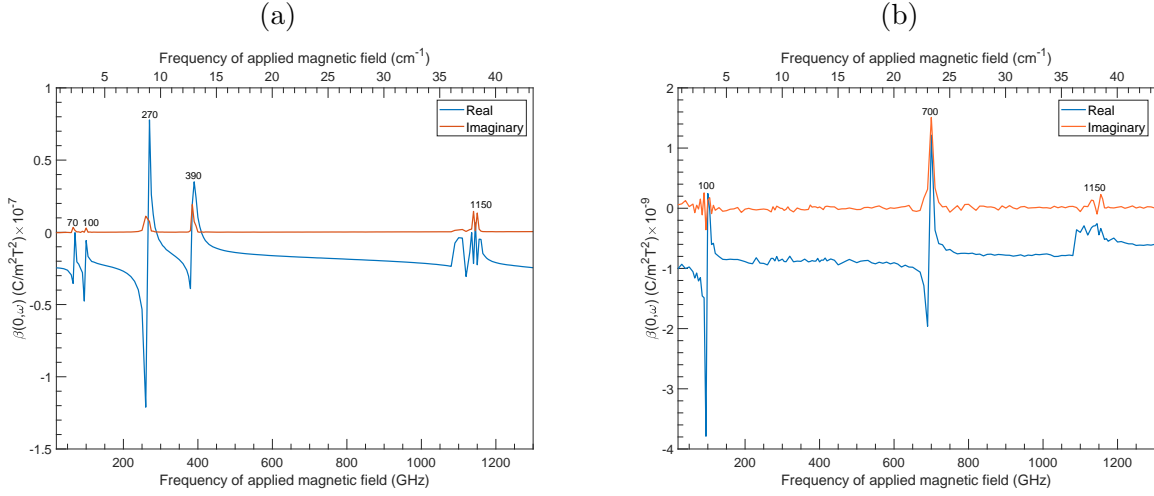


FIG. 3: (Color online) Frequency dependence of the quadratic magnetoelectric coefficient

Frequency dependence of the real and imaginary parts of the quadratic magnetoelectric coefficient  $\beta(0, \omega)$  along the [100] direction (panel a) and the [011] direction (panel b) when the homogeneous strain is unclamped. Note the change of vertical scale between Panels (a) and (b).

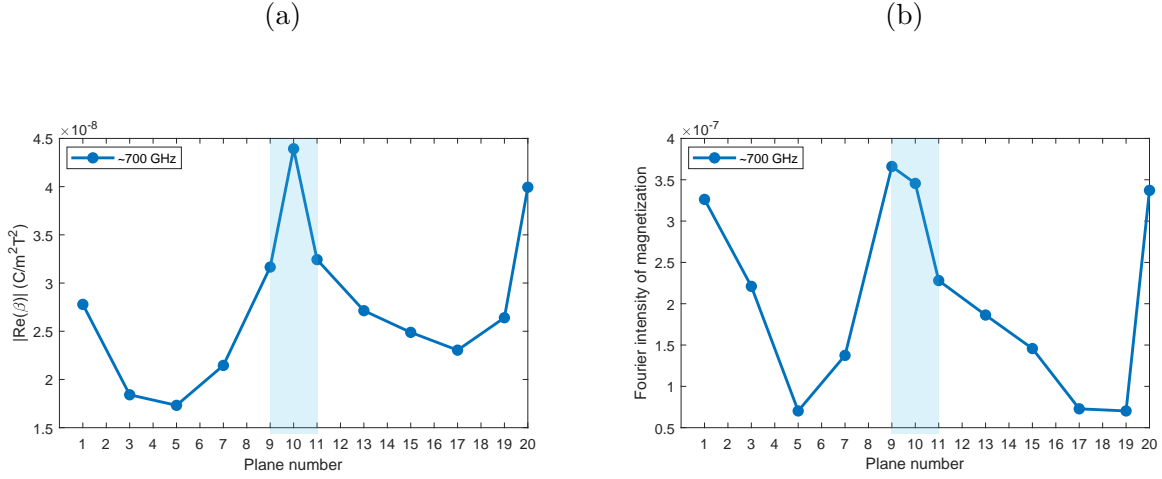


FIG. 4: (Color online) The layer-by-layer analysis for the domain-wall-induced electromagnons at 700 GHz

Layer-by-layer comparison of the intensity of the (a) resonance peaks of the real part of ME coefficient,  $\beta$ , along the  $[011]$  direction when the frequency of applied magnetic field is 700 GHz; (b) Fourier peaks around 700 GHz for magnetization vibrations along the  $[01\bar{1}]$  direction; For panels (b) the frequency of applied magnetic field is 10 GHz.

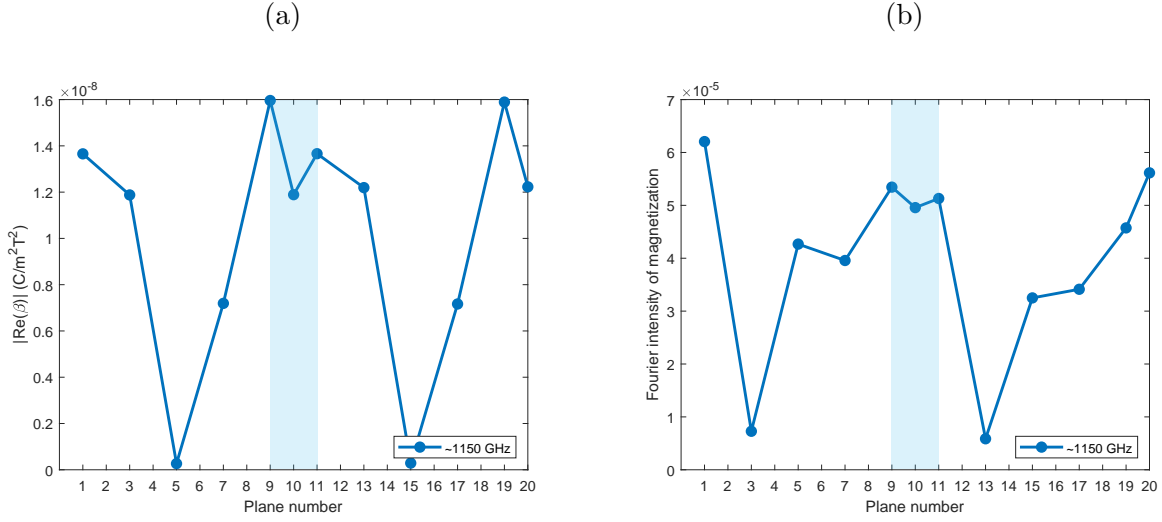


FIG. 5: (Color online) The layer-by-layer analysis for the domain-wall-induced electromagnons at 1150 GHz

Panel (a) shows the magnetolectric coefficient,  $\beta$ , along the  $[100]$  direction when the frequency of applied magnetic field is 1150 GHz; Panels (b) shows the Fourier spectrum of magnetization, along the  $[\bar{2}11]$  direction for 1150 GHz. For panels (b) the frequency of applied magnetic field is 10 GHz.

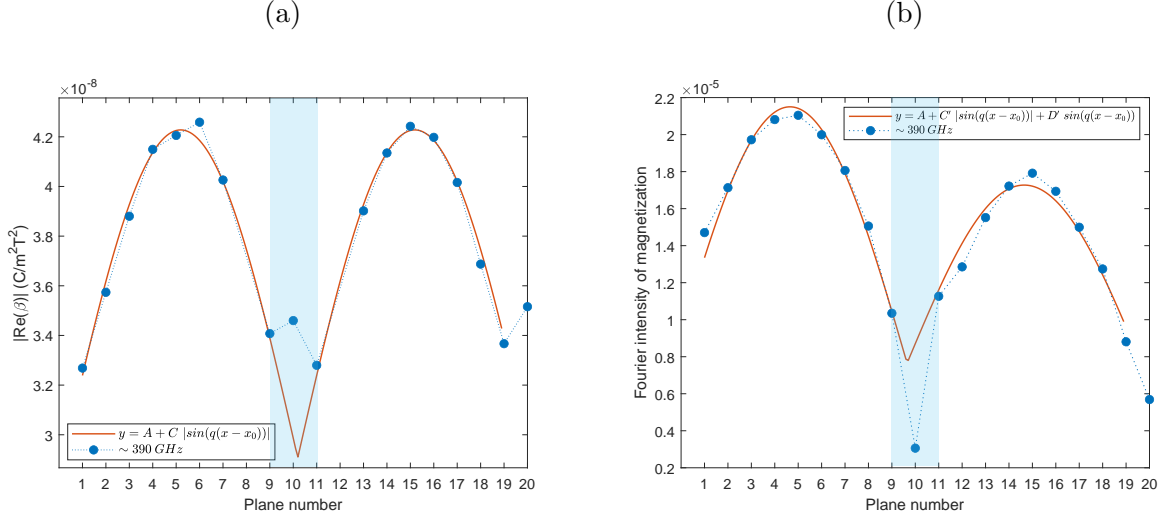


FIG. 6: (Color online) The layer-by-layer analysis for the domain-wall-induced electromagnons at 390 GHz

Layer-by-layer comparison of the intensity of the (a) resonance peaks of the real part of ME coefficient,  $\beta$ , along the  $[100]$  direction when the frequency of applied magnetic field is 390 GHz; (b) Fourier peaks around 390 GHz for magnetization vibrations along the  $[\bar{2}11]$  direction. For panel(b) the frequency of applied magnetic field is 10 GHz.

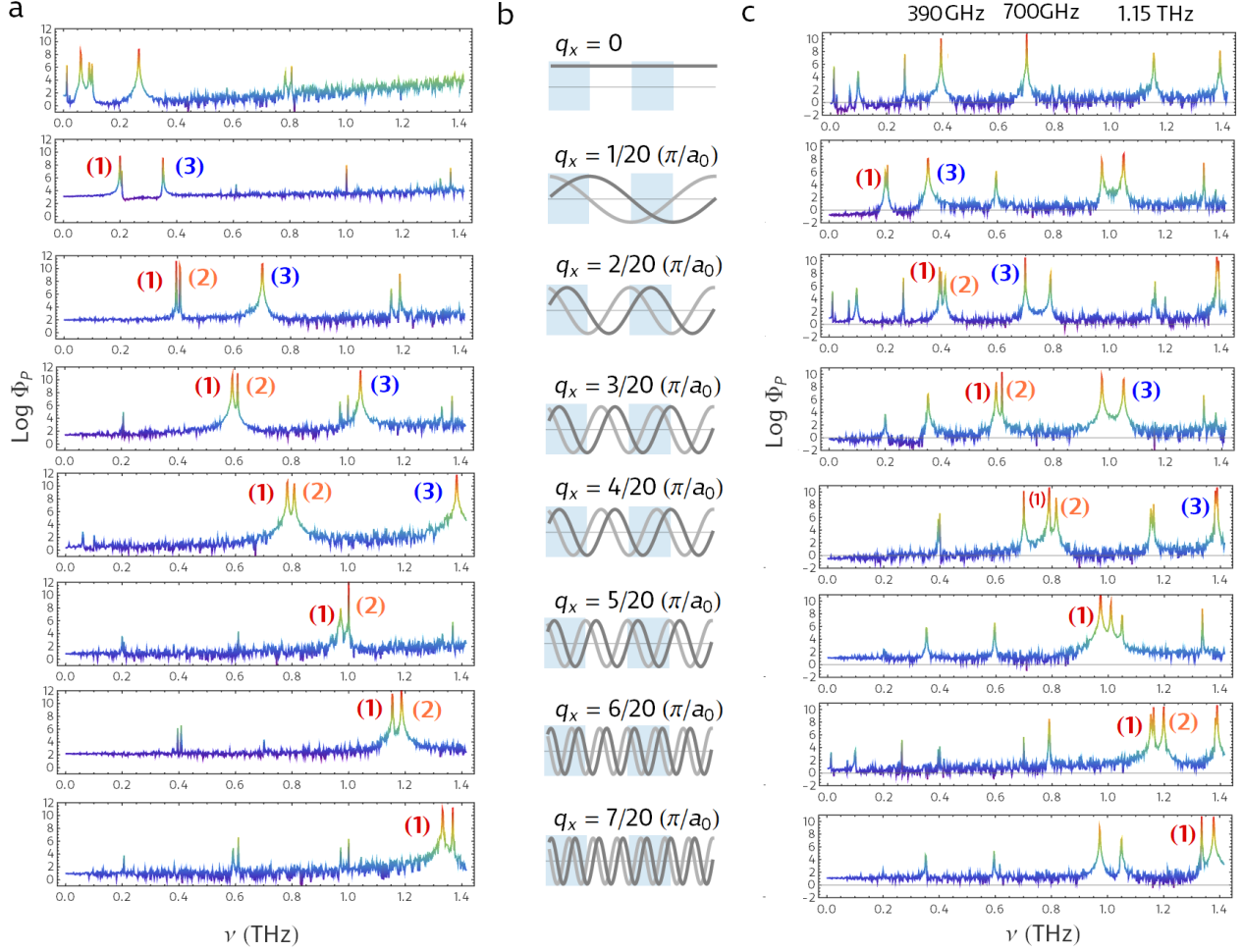


FIG. 7: (Color online) Low-frequency spectrum of polar excitations for monodomain and multidomain states.

Each sub-panel in panels (a) and (c) shows the dependence of the logarithm of the spectral energy density  $\Phi_P$  on frequency at a single wavevectors  $\mathbf{q} = (q_x, 0, 0)$ . The labels (1), (2) and (3) indicate the relevant electromagnon branches. The value of  $q_x$  for each row of sub-panels is indicated in panel (b). Panel (b) also contains a schematic representation of a  $40 \times 10 \times 10$  supercell with four alternating domains (blue and white regions) along with examples of the  $\mathbf{q}$  wave modulations.

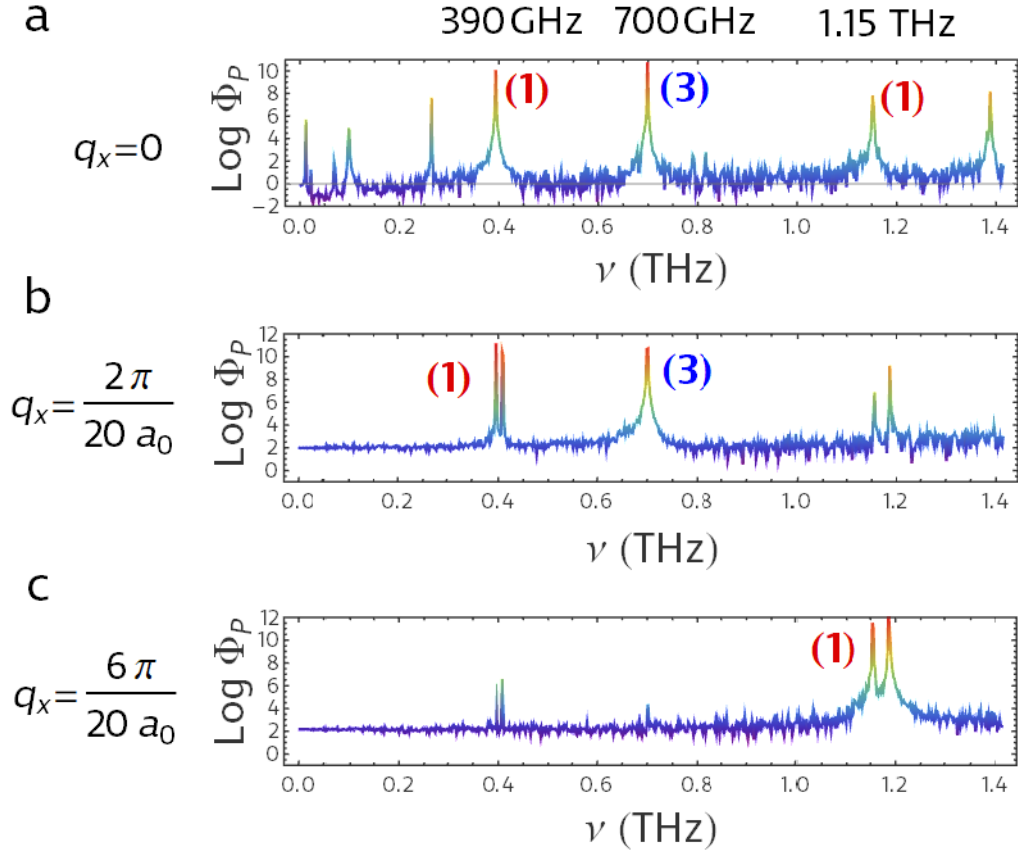


FIG. 8: (Color online) Origin of the zone-center electromagnons.

Panel (a) shows the logarithm of the optical phonon SED at  $q_x = 0$  for the multidomain state.

Panels (b) and (c) shows the logarithm of the optical phonon SED for the monodomain state at

$q_x = \frac{2}{20} \frac{\pi}{a_0}$  and  $q_x = \frac{6}{20} \frac{\pi}{a_0}$ , respectively. Labels (1) and (3) indicate the matching frequencies of

the mode before (panels b,c) and after a single scattering event (panel a).

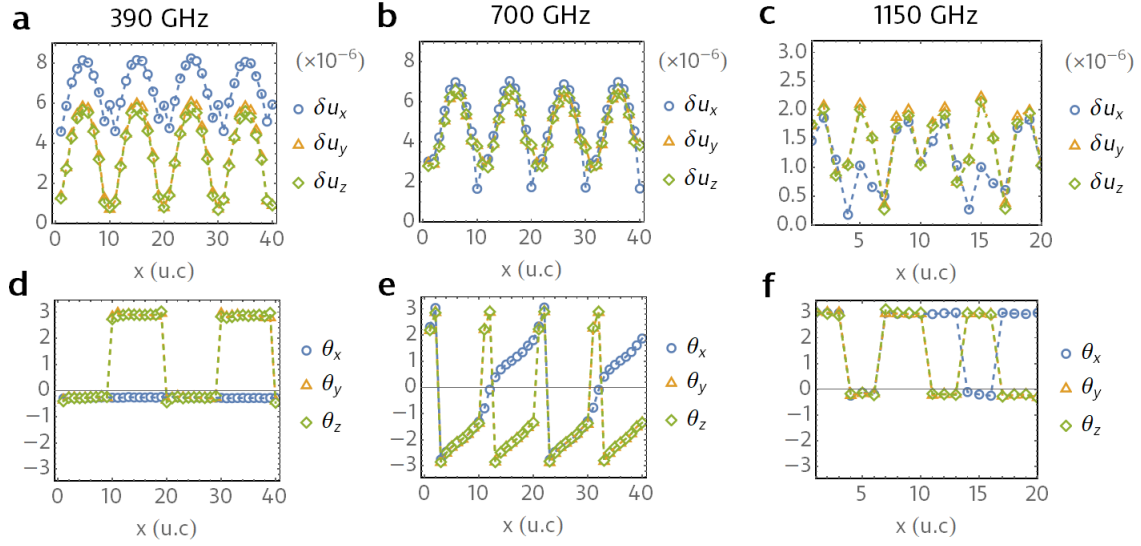


FIG. 9: (Color online) Analysis of local mode vibrations at emergent electromagnon frequencies.

Panels a, b and c (d, e and f) show the changes of the complex amplitude (phase) of the local mode vibrations along the [100] direction at 390 GHz, 700 GHz and 1150 GHz, respectively.

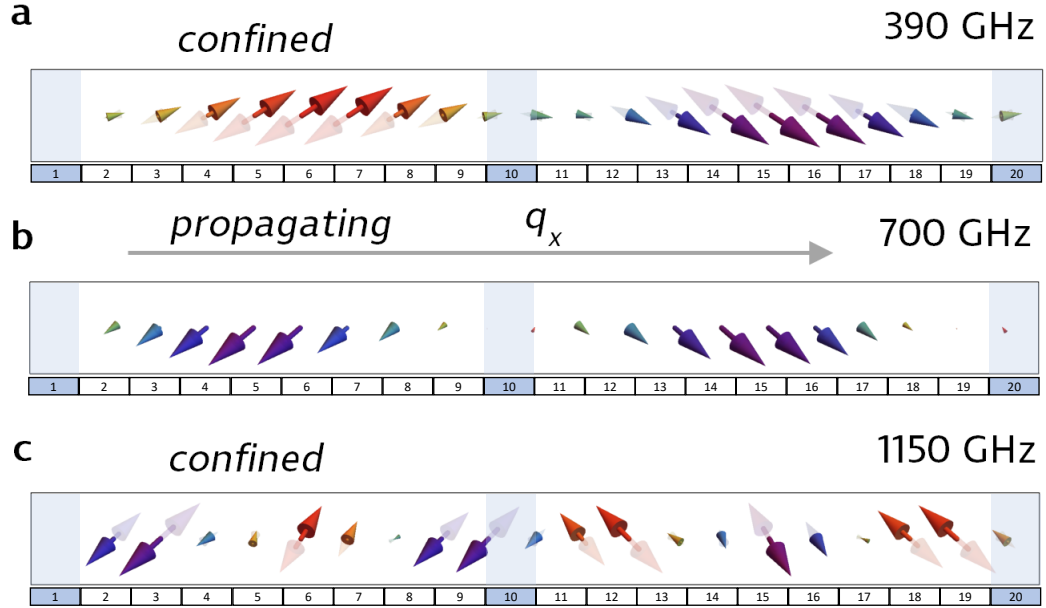


FIG. 10: (Color online) Instantaneous distribution of the local mode deviation vectors for the three considered domain-wall-induced electromagnons.

The arrows indicate the local mode deviations with red (purple) color corresponding to vector with positive (negative)  $z$  components. Electromagnons at 390 GHz and 1150 GHz originate from the same monodomain electromagnon branch and have predominantly confined (standing-wave) character. The 700 GHz domain-wall-induced mode features a pronounced propagating wave nature.